Comput. Methods Appl. Mech. Engrg. 199 (2010) 615–624

Contents lists available at ScienceDirect

Comput. Methods Appl. Mech. Engrg.

journal homepage: www.elsevier.com/locate/cma

Implicit Large Eddy Simulation of non-wall-bounded turbulent flows based on the multiscale properties of a high-order finite volume method

X. Nogueira [a], L. Cueto-Felgueroso [b], I. Colominas [a,*], H. Gómez [a]

[a] Group of Numerical Methods in Engineering, Dept. of Applied Mathematics, Universidade da Coruña, Campus de Elviña, 15071 A Coruña, Spain
[b] Dept. of Civil and Environmental Engineering, Massachusetts Institute of Technology, 77 Massachusetts Ave., Cambridge, MA 02139, USA

ARTICLE INFO

Article history:
Received 8 September 2009
Received in revised form 19 October 2009
Accepted 22 October 2009
Available online 28 October 2009

Keywords:
High-order methods
Moving Least Squares
Turbulence
Compressible flows
Finite volume method

ABSTRACT

In this paper it is presented the application of a higher-order finite volume method based on Moving Least Squares approximations (FV-MLS) to the resolution of non-wall-bounded compressible turbulent flows. Our approach is based on the monotonically implicit Large Eddy Simulation (MILES). The main idea of MILES methodology is the absence of any explicit subgrid scale (SGS) model in the numerical algorithm to solve turbulent flows. In the case of the FV-MLS method, we take advantage of the multiresolution properties of Moving Least Squares Approximations, and we show that they can be used as an implicit SGS model. The numerical results are encouraging. The third-order FV-MLS method is able to reproduce the inertial subrange, and it obtains better results than other usual numerical schemes in LES computations, such as the MUSCL scheme. We note that in the present state of this research, the numerical method is not yet suited for wall-bounded flows. This paper is the first step in the application of the FV-MLS method to general turbulent flows.

1. Introduction

The simulation of turbulent flows still remains as one of the most challenging problems in the field of the computational fluid dynamics. During many years, methods based on Reynolds averaging (RANS) have been the standard method for the computation of engineering problems. Even though this approach is appropriate for analyzing performance, it presents some limitations. Thus, the statistical nature of the solution avoids fine descriptions of unsteady physical mechanisms, and the accuracy of these methods strongly depends on the flow. Moreover, when we average the Navier–Stokes equations, the nature of the equations change. A deterministic phenomenon is expressed in terms of a set of statistic equations. If we accept that the Navier–Stokes equations describe correctly the dynamics of a flow, there is a contradiction with the statistical approach of averaging.

In this context, the Large Eddy Simulation (LES) technique seems to be a more logical approach. In the classical formulation of LES, instead of averaging the equations, we apply a filter. The filter separates the resolved scales from the subgrid (non-resolved) scales. This separation of the scales present in the flow is the main idea of Large Eddy Simulation. Many filters have been used in the literature such as, for example, the box filter [1], the Gaussian filter [2], or temporal filters [3]. The spirit of this approach is to solve the largest scales (the solved scales) of the flow, and model the scales that are not solved.

One of the most widespread model for the subgrid scales is the Smagorinsky model [4]. This model requires the definition of time and length scales, and a constant parameter. However this model is too dissipative, and presents other drawbacks that make the model unsuitable for the simulation of transitional flows. Some of these drawbacks are circumvented with the dynamic Smagorinsky model [5]. In this method, the Smagorinsky constant is replaced with a function of space and time. Thus, the value of this function is updated as the simulation evolves. This methodology uses the information of a part of the large scales of the flow (the smaller scales) to predict the effect of the smallest scales. This model has been extended for use in compressible flows [6,7], and it has been used in many numerical simulations [8,9]. In [10] is introduced the concept of ideal LES subgrid model, in the sense that it will exactly reproduce all single-time, multi-point statistics, with the minimum possible error in instantaneous dynamics. However this ideal subgrid model cannot be computed directly, and thus the optimal LES is defined as the best approximation to ideal LES [11,12].

Most of the drawbacks of the Smagorinsky approach are related to the fact that the subgrid scale model (a turbulent viscosity model) actually affects to both, the solved and unresolved scales, as was pointed out by Hughes et al. [13]. In successive papers [14,15] they introduced a new methodology of LES, the variational multiscale method (VMS). In order to obtain a precise scale separation, they perform a reformulation of the Navier–Stokes equations. In a

---

* Corresponding author.
E-mail address: icolominas@udc.es (I. Colominas).

0045-7825/$ - see front matter © 2009 Elsevier B.V. All rights reserved.
doi:10.1016/j.cma.2009.10.013

recent work Bazilevs et al. [16] proposed another formulation of the VMS method. In this formulation, the fine (subgrid) scales are approximated by an algebraic scaling of the residual of the coarse scale equations. With this approach, no eddy viscosity model is used at all. These two approaches (based on the VMS method) are currently object of extensive research [17–21].

The VMS approach, in its initial formulation is similar in some aspects to the high-pass filtering (HPF) eddy viscosity models [22–24]. These models use an explicit high-pass filtering to separate the highest scales of the solution of the filtered Navier–Stokes equations. Then, a subgrid scale model (subfilter scale, actually) is applied, but using the high-pass filtered variables in the computation of the eddy viscosity instead of the variables resulting from the calculations.

Another approach is the approximated deconvolution model (ADM) [25]. The ADM method tries to reconstruct the unfiltered solution from the filtered solution, by means of an approximated deconvolution and the application of a relaxation term that models the effect of the subgrid scales on the resolved scales. This method can be seen as a consecutive filtering procedure [26].

On the other hand, several authors [27,28] use a multilevel approach based on computations on different grids. The deconvolution of the filtered velocity field is performed on a finer grid, in order to generate the smaller scales to compute the subgrid model. Some authors [27] solve directly on the finer grid, defining the filtering level as two times the grid-spacing of the finest grid.

In Large Eddy Simulations the small scales are removed, and then the energy cascade process is truncated. The energy of the smallest scales solved on the grid can not be transferred to the following scales, producing a pile-up of energy at these scales. Subgrid models introduce the dissipation needed to avoid this effect. Thus, most of the numerical methods developed for LES are based on centered discretizations. These methods do not introduce enough dissipation on uniform grids, and they imperatively need any SGS model. However, upwind methods introduce naturally a certain amount of dissipation. The implicit Large Eddy Simulation (ILES) methods, assume that the action of subgrid scales is purely dissipative [29]. In the context of non-oscillatory finite volume formulations, the Monotone Integrated Large Eddy Simulation (MILES) states the relationship between leading numerical error terms and tensorial subgrid viscosities [30–34]. MILES approach tries to mimic the high-wavenumber end of the inertial subrange. The adaptive flux reconstruction technique establishes a relation between WENO techniques and subgrid viscosity [35]. Even though upwind methods have been recommended for direct numerical simulation (DNS) in complex geometries, the use of these methods for LES is controversial [36–38], due to the excessive dissipation introduced in coarse grids. One of the objectives of this work is to show that it is possible to develop upwind schemes for turbulent flows without introducing excessive dissipation on coarse grids. A drawback of the MILES approach is the lack of a solid physical basis. In this aspect, the first steps have been developed [39].

The ILES approach is not only related to upwind schemes. Thus, the compact finite difference plus explicit filtering approach [40–42] may also be considered as an ILES procedure. In this methodology, a very accurate compact finite difference discretization is used with an explicit Padé filter. The parameter of the filter is chosen by a stability criterion. The so called adaptive DNS/LES method has been used in the context of adaptive stabilized Galerkin finite element methods [43]. On the other hand, it has been proposed the use of spectral vanishing viscosities for spectral methods [44,45].

In this work we propose the use of a third-order finite volume scheme based on Moving Least Squares approximations (FV-MLS) [46–48] for the simulation of non-wall-bounded turbulent flows in an ILES framework. We use one free parameter of the scheme (related to the shape of a kernel function) to control the filtering procedure. This parameter can be used to modify the dispersion and dissipation characteristics of the FV-MLS method, changing the behavior of the numerical scheme. In practice, the filtering operation is performed in the approximation of the derivatives, thus it can be considered as an implicit filtering. Differently from other implicit-LES finite volume schemes, the present approach allows the modification of the shape of the implicit filter by changing the value of the shape parameter. This provides a certain degree of decoupling between the mesh spacing and the implicit filter width.

The main goal of this paper is to examine the accuracy of the third-order FV-MLS method in the resolution of compressible turbulent flows. The paper is structured as follows: In Section 2 we expose the 3D Navier–Stokes equations. In Section 3 we present the formulation of the numerical method to solve that set of equations, and in Section 4 we test the FV-MLS method in the Large Eddy Simulation of the decay of isotropic compressible turbulence. Finally, in Section 5, we draw the conclusions.

2. The Navier–Stokes equations

The 3D Navier–Stokes equations written in conservative form read as:

$$\frac{\partial \boldsymbol{U}}{\partial t}+\frac{\partial\left(\boldsymbol{F}_x-\boldsymbol{F}_x^V\right)}{\partial x}+\frac{\partial\left(\boldsymbol{F}_y-\boldsymbol{F}_y^V\right)}{\partial y}+\frac{\partial\left(\boldsymbol{F}_z-\boldsymbol{F}_z^V\right)}{\partial z}=0 \tag{1}$$

with

$$\boldsymbol{U}=\begin{pmatrix}\rho\\ \rho v_x\\ \rho v_y\\ \rho v_z\\ \rho E\end{pmatrix}, \tag{2}$$

$$\boldsymbol{F}_x=\begin{pmatrix}\rho v_x\\ \rho v_x^2+p\\ \rho v_x v_y\\ \rho v_x v_z\\ \rho v_x H\end{pmatrix}\quad \boldsymbol{F}_y=\begin{pmatrix}\rho v_y\\ \rho v_x v_y\\ \rho v_y^2+p\\ \rho v_y v_z\\ \rho v_y H\end{pmatrix}\quad \boldsymbol{F}_z=\begin{pmatrix}\rho v_z\\ \rho v_x v_z\\ \rho v_y v_z\\ \rho v_z^2+p\\ \rho v_z H\end{pmatrix}, \tag{3}$$

$$\boldsymbol{F}_x^V=\begin{pmatrix}0\\ \tau_{xx}\\ \tau_{xy}\\ \tau_{xz}\\ v_x\tau_{xx}+v_y\tau_{xy}+v_z\tau_{xz}-q_x\end{pmatrix}$$

$$\boldsymbol{F}_y^V=\begin{pmatrix}0\\ \tau_{xy}\\ \tau_{yy}\\ \tau_{yz}\\ v_x\tau_{xy}+v_y\tau_{yy}+v_z\tau_{yz}-q_y\end{pmatrix} \tag{4}$$

$$\boldsymbol{F}_z^V=\begin{pmatrix}0\\ \tau_{xz}\\ \tau_{yz}\\ \tau_{zz}\\ v_x\tau_{xz}+v_y\tau_{yz}+v_z\tau_{zz}-q_z\end{pmatrix},$$

$$\rho E=\rho e+\frac{1}{2}\rho(\boldsymbol{v}\cdot\boldsymbol{v}), \tag{5}$$

$$H=E+\frac{p}{\rho}. \tag{6}$$

where ρ is the density, $\boldsymbol{v}=(v_x,v_y,v_z)$ is the velocity, μ is the effective viscosity of the fluid, H is the enthalpy, E is the total energy, e is the internal energy and ρ is the density. The viscous stress tensor is defined as,

$$\tau_{xx} = 2\mu\frac{\partial v_x}{\partial x} - \frac{2}{3}\mu\left(\frac{\partial v_x}{\partial x} + \frac{\partial v_y}{\partial y} + \frac{\partial v_z}{\partial z}\right),$$

$$\tau_{yy} = 2\mu\frac{\partial v_y}{\partial y} - \frac{2}{3}\mu\left(\frac{\partial v_x}{\partial x} + \frac{\partial v_y}{\partial y} + \frac{\partial v_z}{\partial z}\right), \tag{7}$$

$$\tau_{zz} = 2\mu\frac{\partial v_z}{\partial z} - \frac{2}{3}\mu\left(\frac{\partial v_x}{\partial x} + \frac{\partial v_y}{\partial y} + \frac{\partial v_z}{\partial z}\right), \tag{8}$$

$$\tau_{xy} = \mu\left(\frac{\partial v_x}{\partial y} + \frac{\partial v_y}{\partial x}\right),$$

$$\tau_{xz} = \mu\left(\frac{\partial v_x}{\partial z} + \frac{\partial v_z}{\partial x}\right),$$

$$\tau_{yz} = \mu\left(\frac{\partial v_y}{\partial z} + \frac{\partial v_z}{\partial y}\right). \tag{9}$$

Thermal flux $\boldsymbol{q} = (q_x, q_y, q_z)$, is computed using Fourier's law:

$$q_x = -\lambda\frac{\partial T}{\partial x} \quad q_y = -\lambda\frac{\partial T}{\partial y} \quad q_z = -\lambda\frac{\partial T}{\partial z}, \tag{10}$$

where λ is the thermal conductivity.

We assume that the viscosity depends on the temperature following Sutherland's law:

$$\mu = \mu_\infty\frac{T_{ref} + S_0}{T + S_0}\left(\frac{T}{T_{ref}}\right)^{1.5}, \tag{11}$$

where T_{ref} is a reference temperature and $S_0 = 110.4$ K is an empirical constant (Sutherland's temperature).

3. Numerical method: a MLS-based finite volume scheme

A method based on the application of Moving Least Squares [49] to compute the derivatives in a finite volume framework (FV-MLS) has been developed in 2D in [46,47]. In this work we extend the formulation to 3D, to compute the 3D Navier–Stokes equations for the first time with this numerical method. In order to increase the order achieved by the finite volume method, a Taylor expansion of the variable is performed at the interior of each cell. The approximation of the higher-order derivatives needed to compute the Taylor reconstruction is obtained by a Moving Least Squares approach.

3.1. General formulation

Consider a system of conservation laws of the form

$$\frac{\partial \boldsymbol{U}}{\partial t} + \nabla\cdot(\mathscr{F}^H + \mathscr{F}^E) = \boldsymbol{S} \quad \text{in} \quad \Omega, \tag{12}$$

and a suitable set of initial and boundary conditions. The fluxes have been generically split into a hyperbolic-like part, $\mathscr{F}^H$, and an elliptic-like part, $\mathscr{F}^E$.

We divide the domain Ω into a set of non-overlapping *control volumes* or *cells*. Furthermore, we define a reference point (*node*), $\boldsymbol{x}_I$ inside each cell I. In our case, the reference point is identified with the cell centroid.

The integral form of 12 which, for each control volume I, reads

$$\int_{\Omega_I}\frac{\partial \boldsymbol{U}}{\partial t}\,d\Omega + \int_{\Gamma_I}(\mathscr{F}^H + \mathscr{F}^E)\boldsymbol{n}\,d\Gamma = \int_{\Omega_I}\boldsymbol{S}\,d\Omega. \tag{13}$$

Introducing the component-wise reconstructed function $\boldsymbol{u}^h$, the spatially discretized counterpart of 13 reads

$$\int_{\Omega_I}\frac{\partial \boldsymbol{U}^h}{\partial t}\,d\Omega + \int_{\Gamma_I}(\mathscr{F}^{hH} + \mathscr{F}^{hE})\boldsymbol{n}\,d\Gamma = \int_{\Omega_I}\boldsymbol{S}^h\,d\Omega. \tag{14}$$

We use Moving Least Squares (MLS) [49] approximants to build the spatial representation of the solution. This approximation gives us a continuous, highly-accurate and centered representation of the solution. Thus, a direct evaluation of the fluxes is possible, and in fact, it is efficient when the problem is not predominantly hyperbolic. For convection-dominated problems, we use a different approximation for hyperbolic and elliptic terms. Thus, for hyperbolic terms we introduce a "*broken*" reconstruction, $\boldsymbol{U}_I^{hb}$, which approximates $\boldsymbol{U}^h(\boldsymbol{x})$ locally inside each cell I, and is discontinuous across cell interfaces [46]. This approximation allows us to use the powerful and efficient Riemann solvers technology, limiters and other finite volume techniques. In general, the order of accuracy of the broken reconstruction has to be the same as that of the original continuous reconstruction, that is:

$$\left|\boldsymbol{U}(x) - \boldsymbol{U}^h(\boldsymbol{x})\right| \leqslant C_1 h^{k+1}, \tag{15}$$

and

$$\left|\boldsymbol{U}(\boldsymbol{x}) - \boldsymbol{U}_I^{hb}(\boldsymbol{x})\right| \leqslant C_2 h^{k+1}, \tag{16}$$

for some constants k, C_1, C_2 and a characterisitc cell size h. As we will show later, one possible choice is to use Taylor series expansions (see Section 3.3, Eq. (33)).

On the other hand, the MLS continuous reconstruction is used to evaluate directly the elliptic terms at integration points.

The final semidiscrete scheme for the continuous/discontinuous approach can be written as

$$\int_{\Omega_I}\frac{\partial \boldsymbol{U}^h}{\partial t}\,d\Omega + \int_{\Gamma_I}\boldsymbol{H}(\boldsymbol{U}^{hb+}, \boldsymbol{U}^{hb-})\,d\Gamma + \int_{\Gamma_I}\mathscr{F}^{hE}\boldsymbol{n}\,d\Gamma = \int_{\Omega_I}\boldsymbol{S}^h\,d\Omega, \tag{17}$$

where $\boldsymbol{H}(\boldsymbol{U}^{hb+}, \boldsymbol{U}^{hb-})$ is a suitable numerical flux.

3.2. Moving Least Squares (MLS) approximation

For clarity, in the following exposition, we consider a single variable u, instead of the vector-variable U. If we consider a function $u(\boldsymbol{x})$ defined in a domain Ω, the basic idea of the MLS approach is to approximate $u(\boldsymbol{x})$, at a given point $\boldsymbol{x}$, through a weighted least squares fitting of $u(\boldsymbol{x})$ in a neighborhood of $\boldsymbol{x}$ as

$$u(\boldsymbol{x}) \approx u^h(\boldsymbol{x}) = \sum_{i=1}^{m} p_i(\boldsymbol{x})\alpha_i(\boldsymbol{z})|_{\boldsymbol{z}=\boldsymbol{x}} = \boldsymbol{p}^T(\boldsymbol{x})\boldsymbol{\alpha}(\boldsymbol{z})|_{\boldsymbol{z}=\boldsymbol{x}}. \tag{18}$$

$\boldsymbol{p}^T(\boldsymbol{x})$ is a (usually) polynomial basis and $\boldsymbol{\alpha}(\boldsymbol{z})|_{\boldsymbol{z}=\boldsymbol{x}}$ is a set of parameters to be determined, such that they minimize the following error functional:

$$J(\boldsymbol{\alpha}(\boldsymbol{z})|_{\boldsymbol{z}=\boldsymbol{x}}) = \int_{\boldsymbol{y}\in\Omega_{\boldsymbol{x}}} W(\boldsymbol{z}-\boldsymbol{y}, h)|_{\boldsymbol{z}=\boldsymbol{x}}\left[u(\boldsymbol{y}) - \boldsymbol{p}^T(\boldsymbol{y})\boldsymbol{\alpha}(\boldsymbol{z})|_{\boldsymbol{z}=\boldsymbol{x}}\right]^2 d\Omega_{\boldsymbol{x}}, \tag{19}$$

where $W(\boldsymbol{z}-\boldsymbol{y}, h)|_{\boldsymbol{z}=\boldsymbol{x}}$ is a *kernel* with compact support (denoted by $\Omega_{\boldsymbol{x}}$) centered at $\boldsymbol{z} = \boldsymbol{x}$. The parameter h is the smoothing length, which is a measure of the size of the support $\Omega_{\boldsymbol{x}}$ [46]. The role of the kernel is to weight the importance of the different points used for the approximation. The minimization of J gives the following:

$$\int_{\boldsymbol{y}\in\Omega_{\boldsymbol{x}}} \boldsymbol{p}(\boldsymbol{y})W(\boldsymbol{z}-\boldsymbol{y}, h)|_{\boldsymbol{z}=\boldsymbol{x}}u(\boldsymbol{y})d\Omega_{\boldsymbol{x}} = \boldsymbol{M}(\boldsymbol{x})\boldsymbol{\alpha}(z)|_{\boldsymbol{z}=\boldsymbol{x}}, \tag{20}$$

where the moment matrix $\boldsymbol{M}(\boldsymbol{x})$ is defined as

$$\boldsymbol{M}(\boldsymbol{x}) = \int_{\boldsymbol{y}\in\Omega_{\boldsymbol{x}}} \boldsymbol{p}(\boldsymbol{y})W(\boldsymbol{z}-\boldsymbol{y}, h)|_{\boldsymbol{z}=\boldsymbol{x}}\boldsymbol{p}^T(\boldsymbol{y})d\Omega_{\boldsymbol{x}}. \tag{21}$$

Integrals in 20 and 21 are evaluated using the nodes in $\Omega_{\boldsymbol{x}}$ ($n_{\boldsymbol{x}}$) as quadrature points, to obtain the following value of $\boldsymbol{\alpha}$

$$\boldsymbol{\alpha}(z)|_{\boldsymbol{z}=\boldsymbol{x}} = \boldsymbol{M}^{-1}(\boldsymbol{x})\mathbf{P}_{\Omega_{\boldsymbol{x}}}\boldsymbol{W}(\boldsymbol{x})\boldsymbol{U}_{\Omega_{\boldsymbol{x}}}, \tag{22}$$

where the matrix

$$\mathbf{u}_{\Omega_x} = \left(u(\mathbf{x}_1)\ldots u(\mathbf{x}_{n_{\mathbf{x}_I}})\right), \tag{23}$$

contains the nodal values of $u(\mathbf{x})$ associated to the $n_{\mathbf{x}}$ nodes in $\Omega_{\mathbf{x}}$ (Fig. 1). In the above, $n_{\mathbf{x}_I}$ is the number of neighbors of the cell I.

Thus, the discrete expression of the moment matrix is $\mathbf{M} = \mathbf{p}_{\Omega_{\mathbf{x}}} W(\mathbf{x}) \mathbf{p}_{\Omega_{\mathbf{x}}}^T$ (see [46]).

We also define the matrices (see [46]):

$$\mathbf{p}_{\Omega_x} = \left(p(\mathbf{x}_1)\cdots p(\mathbf{x}_{n_{\mathbf{x}_I}})\right), \tag{24}$$

and

$$W(\mathbf{x}) = diag(W_i(\mathbf{x})) \quad i = 1,\ldots,n_{\mathbf{x}_I}. \tag{25}$$

From a practical point of view, for each point I we need to define a set of neighbors inside the compact support $\Omega_{\mathbf{x}}$. The minimum number of neighbors is determined by the number of functions in the polynomial basis $\mathbf{p}(\mathbf{x})$.

Following [46], the interpolation structure can be identified as

$$u_I^h(\mathbf{x}) = \mathbf{p}^T(\mathbf{x})\boldsymbol{\alpha}(\mathbf{z})|_{\mathbf{z}=\mathbf{x}} = \mathbf{p}^T(\mathbf{x})\mathbf{M}^{-1}(\mathbf{x})\mathbf{p}_{\Omega_{\mathbf{x}}}\mathbf{W}(\mathbf{x})\mathbf{u}_{\Omega_{\mathbf{x}}} = N^T(\mathbf{x})\mathbf{u}_{\Omega_{\mathbf{x}}}. \tag{26}$$

The MLS "shape functions" are defined as:

$$\mathbf{N}^{\mathbf{T}}(\mathbf{x}) = \mathbf{p}^T(\mathbf{x})\mathbf{M}^{-1}(\mathbf{x})\mathbf{p}_{\Omega_{\mathbf{x}}}\mathbf{W}(\mathbf{x}), \tag{27}$$

and finally we can write:

$$u_I^h(\mathbf{x}) = \sum_{j=1}^{n_{\mathbf{x}_I}} N_j(\mathbf{x}) u_j. \tag{28}$$

The approximation is written in terms of the MLS "shape functions" $\mathbf{N}^T(\mathbf{x})$.

In this work the following polynomial cubic basis is used:

$$\mathbf{p}(\mathbf{x}) = \left(1,x,y,z,xy,xz,yz,x^2,y^2,z^2,x^2y,x^2z,y^2x,y^2z,z^2x,\right.\\ \left. z^2y,xyz,x^3,y^3,z^3\right), \tag{29}$$

where (x,y,z) are the Cartesian coordinates of vector $\mathbf{x}$.

In order to improve the conditioning, the polynomial basis is locally defined and scaled: if the shape functions are evaluated at $\mathbf{x}_I$, the polynomial basis is evaluated at $(\mathbf{x}-\mathbf{x}_I)/h$. With this coordinate transformation, the MLS shape functions can be written as:

$$\mathbf{N}^T(\mathbf{x}) = \mathbf{p}^T(\mathbf{0})\mathbf{C}(\mathbf{x}_I) = \mathbf{p}^T(\mathbf{0})\mathbf{M}^{-1}(\mathbf{x}_I)\mathbf{p}_{\Omega_{\mathbf{x}_I}}\mathbf{W}(\mathbf{x}_I), \tag{30}$$

with

$$\mathbf{C}(\mathbf{x}) = \mathbf{M}^{-1}(\mathbf{x})\mathbf{P}_{\Omega_x}\mathbf{W}(\mathbf{x}). \tag{31}$$

The derivatives of $\mathbf{N}^T(\mathbf{x})$ can be used to compute an approximation to the derivatives of the function. So, the gradient of $\mathbf{U}^h(\mathbf{x})$ at cell I is evaluated as

$$\nabla u_I^h(\mathbf{x}) = \sum_{j=1}^{n_{\mathbf{x}_I}} u_j \nabla N_j(\mathbf{x}). \tag{32}$$

More details about the FV-MLS method can be found in [46,47].

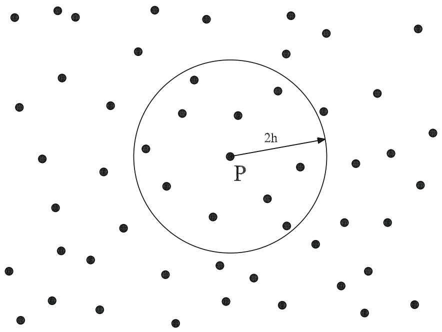

Fig. 1. Meshfree approximation: general scheme. Support for reconstruction at P.

3.3. Application to Navier–Stokes equations

In the context of generalized Godunov's methods we use Eq. (32) to compute the first and second derivatives required for the Taylor reconstruction of the variables at quadrature points at the edges. In case of unsteady problems, this reconstruction needs to use correction terms in order to ensure that the average value of the reconstructed variables over a cell I is the centroid value $\mathbf{U}_I$ [46,47,50]. The resulting scheme is a third-order method.

Thus, the *"broken"* reconstruction, $\mathbf{U}_I^{hb}$, which approximates $\mathbf{U}^h(\mathbf{x})$ locally inside each cell I reads as:

$$\mathbf{U}_I^{hb}(\mathbf{x}) = \mathbf{U}_I^h + \nabla\mathbf{U}_I^h \cdot (\mathbf{x}-\mathbf{x}_I) + \frac{1}{2}(\mathbf{x}-\mathbf{x}_I)^T\mathbf{H}_I(\mathbf{x}-\mathbf{x}_I), \tag{33}$$

where the gradient $\nabla\mathbf{U}_I^h$ and the Hessian matrix $\mathbf{H}_I$ involve the successive derivatives of the continuous reconstruction $\mathbf{U}^h(\mathbf{x})$, which are evaluated at the cell centroids using MLS. In order to ensure the conservation of the mean value, we need to add some correction terms, and the reconstruction reads:

$$\begin{aligned}\mathbf{U}_I^{hb}(\mathbf{x}) &\\ = \mathbf{U}_I^h &+ \nabla\mathbf{U}_I^h \cdot (\mathbf{x}-\mathbf{x}_I) + \frac{1}{2}(\mathbf{x}-\mathbf{x}_I)^T\mathbf{H}_I(\mathbf{x}-\mathbf{x}_I)\\ &- \frac{1}{2V_I}\left[I_{xx}\frac{\partial^2\mathbf{U}_I^h}{\partial x^2} + 2I_{xy}\frac{\partial^2\mathbf{U}_I^h}{\partial x\partial y} + 2I_{xz}\frac{\partial^2\mathbf{U}_I^h}{\partial x\partial z} + 2I_{yz}\frac{\partial^2\mathbf{U}_I^h}{\partial y\partial z}\right.\\ &\left. + I_{yy}\frac{\partial^2\mathbf{U}_I^h}{\partial y^2} + I_{zz}\frac{\partial^2\mathbf{U}_I^h}{\partial z^2}\right],\end{aligned} \tag{34}$$

with:

$$\begin{aligned}&I_{xx} = \int_\Omega (x-x_I)^2 d\Omega, \quad I_{yy} = \int_\Omega (y-y_I)^2 d\Omega, \quad I_{zz} = \int_\Omega (z-z_I)^2 d\Omega\\ &I_{xy} = \int_\Omega (x-x_I)(y-y_I) d\Omega, \quad I_{xz} = \int_\Omega (x-x_I)(z-z_I) d\Omega\\ &I_{yz} = \int_\Omega (y-y_I)(z-z_I) d\Omega\end{aligned} \tag{35}$$

and V_I is the volume of the control volume I.

In order to impose the monotonicity of the high-order method, we use a shock detection technique based on the multiresolution properties of Moving Least Squares applied together with a classical slope limiter [48]. Here we have chosen the Barth and Jespersen limiter [51].

A very interesting feature of the proposed numerical method is the discretization of viscous terms. Moving Least Squares

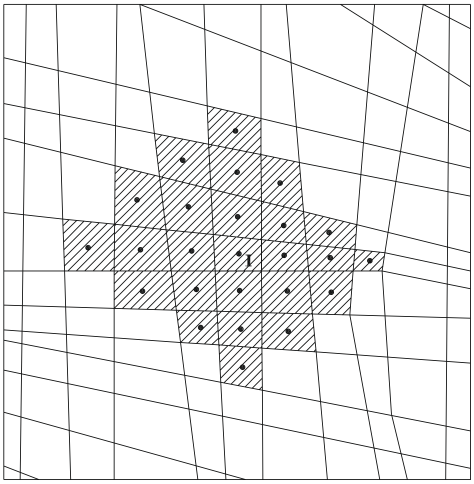

Fig. 2. Full FV-MLS stencil for the 2D Navier–Stokes equations for a cell I. It is the union of the MLS stencil of cell I and the MLS stencils of its first neighbors.

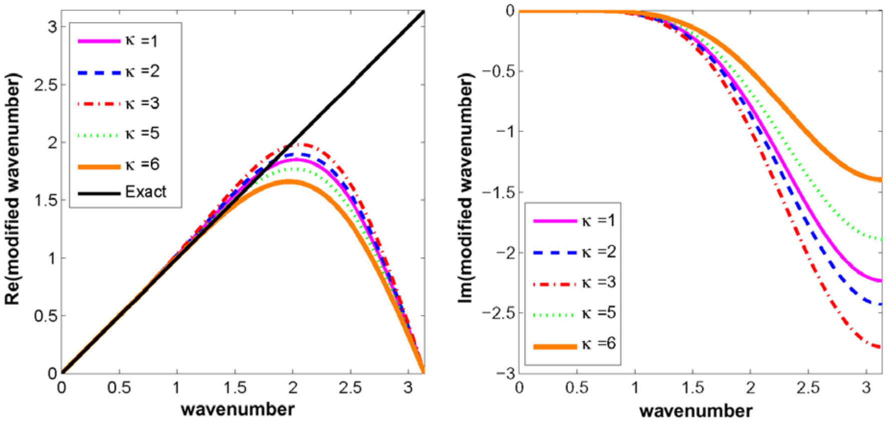

Fig. 3. Dispersion (left) and dissipation (right) curves of the third-order FV-MS scheme, for different values of the kernel shape parameter κ_x.

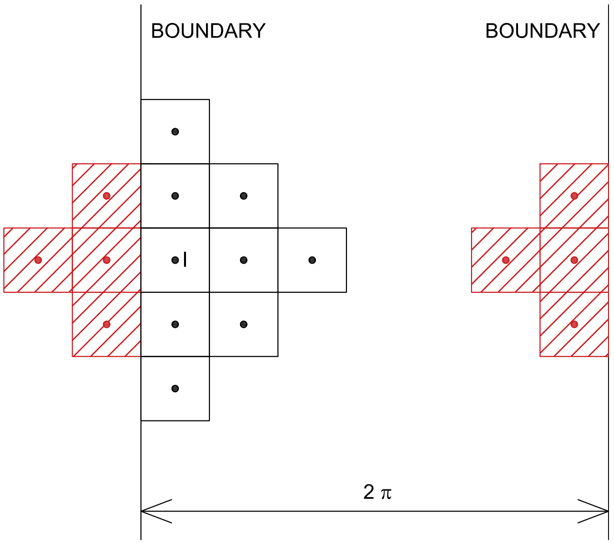

Fig. 4. Modification of the stencil for periodic boundary conditions. Shaded cells in the stencil of cell *I* are substituted by the corresponding shaded cells in the opposite face.

approximations perform a centered, high-accurate and *direct* approximation of viscous fluxes at the quadrature points of the edges. Thus, focusing on the Navier–Stokes equations, the evaluation of the viscous stresses and heat fluxes requires interpolating the velocity vector $\boldsymbol{v}$, temperature T, and their corresponding gradients, $\nabla \boldsymbol{v}$ and ∇T, at each quadrature point $\boldsymbol{x}_{iq}$. Using MLS approximation, these entities are readily computed as

$$v_{iq} = \sum_{j=1}^{n_{iq}} \boldsymbol{v}_j N_j(\boldsymbol{x}_{iq}), \quad T_{iq} = \sum_{j=1}^{n_{iq}} T_j N_j(\boldsymbol{x}_{iq}), \tag{36}$$

and

$$\nabla \boldsymbol{v}_{iq} = \sum_{j=1}^{n_{iq}} \boldsymbol{v}_j \otimes \nabla N_j(x_{iq}), \quad \nabla T_{iq} = \sum_{j=1}^{n_{iq}} T_j \nabla N_j(\boldsymbol{x}_{iq}), \tag{37}$$

where n_{iq} is the number of neighbor centroids given by the stencil.

We need to identify the neighboring points of each node. In fixed grids, this is done once at the beginning of the computations. In Fig. 2 we plot the full 2D stencil of a FV-MLS method with cubic polynomial basis. It is the union of the MLS stencil of cell *I* and the MLS stencils of its first neighbors. The extension to 3D is straightforward, and it is done following the same rationale.

More details about the FV-MLS method can be found in [46,47].

3.4. Exponential kernel: dispersion and dissipation characteristics

It is possible to use different kernels for the definition of shape functions [52]. We have considered here the following exponential kernel:

$$W(x, x^*, \kappa_x) = \frac{e^{-\left(\frac{s}{c}\right)^2} - e^{-\left(\frac{d_m}{c}\right)^2}}{1 - e^{-\left(\frac{d_m}{c}\right)^2}}, \tag{38}$$

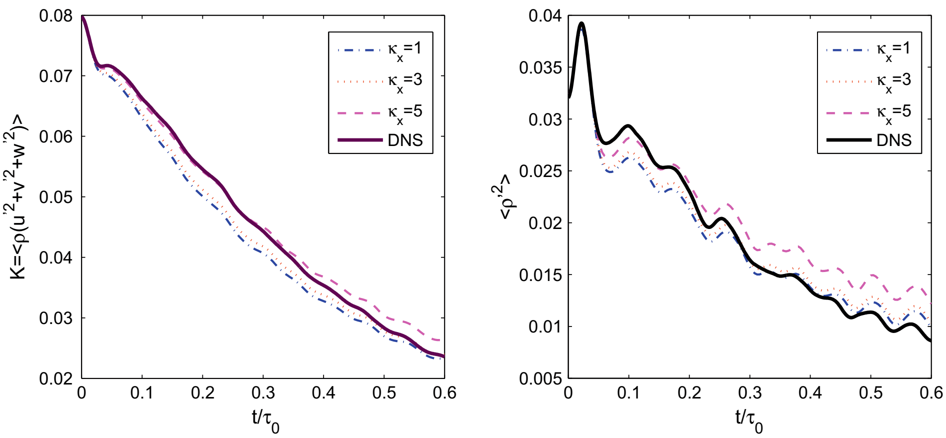

Fig. 5. Effect of the shape parameter κ_x on time history of turbulent kinetic energy decay (left), and on time history of density fluctuations (right). Results for the 32^3 mesh.

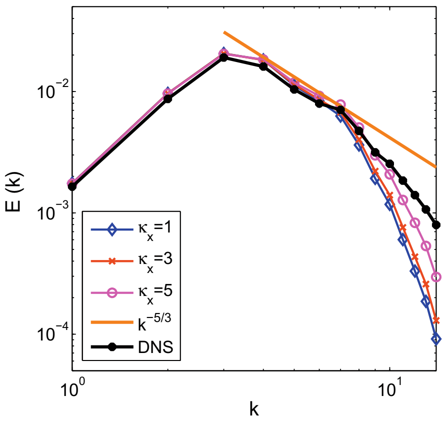

Fig. 6. Instantaneous three-dimensional energy spectra at $t/\tau_0 = 0.3$. Effect of the shape parameter κ_x. Results for the 32^3 mesh.

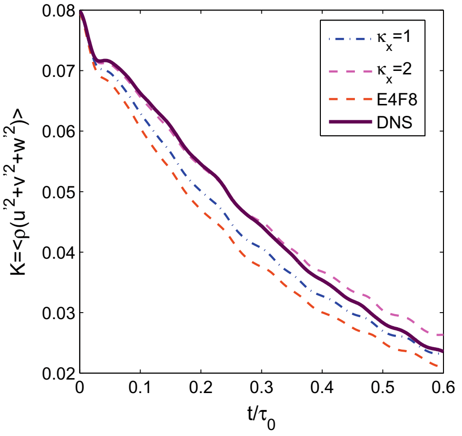

Fig. 7. Time history of turbulent kinetic energy decay. Comparison between third-order FV-MLS results and a centered fourth-order finite differences method with a eighth-order filter [42]. Results for the 32^3 mesh.

with $s = |x_j - x^*|, d_m = 2\max(|x_j - x^*|)$, with $j = 1, \ldots, n_x^*, c = \frac{d_m}{\kappa_x}$, x is the position of every cell centroid of the stencil and κ_x is a shape parameter.

A multidimensional kernel is obtained by multiplying 1D kernels corresponding to each direction. Thus, the 3D exponential kernel reads:

$$W_j(\boldsymbol{x}, \boldsymbol{x}^*, \kappa_x, \kappa_y, \kappa_z) = W_j(x, x^*, \kappa_x) W_j(y, y^*, \kappa_y) W_j(z, z^*, \kappa_z). \qquad (39)$$

For all the computations in this paper we use an isotropic kernel, that is, $\kappa = \kappa_x = \kappa_y = \kappa_z$. The kernel plays a crucial role on the properties of the FV-MLS scheme. In Fig. 3 we plot the dispersion and dissipation curves of the third-order FV-MLS scheme for the 1D advection equation. In these figures we plot the real wavenumber versus the real part of the modified wavenumber (related to dispersion errors), and versus the imaginary part of the modified wavenumber (related to dissipation errors). In this figure, no dissipation is indicated by a zero value of the imaginary part. These figures show that the discrete differential operator is not able to reproduce exactly all the range of frequencies of a given wave, introducing both dispersion and dissipation errors.

We observe that a different choice of the value of the shape parameter of the kernel leads to different characteristics of the scheme. The accurate resolution of the hyperbolic terms of the Navier–Stokes equations is crucial in order to obtain an accurate solution. Thus, the interest of these figures is to show what we can expect of the third-order FV-MLS method when dealing with hyperbolic terms. It is obvious that these curves do not try to reproduce the behavior of the FV-MLS when dealing with the 3D Navier–Stokes equations, since they are non-linear, multidimensional and not strictly hyperbolic. However, the curves can help to understand how the shape parameter acts as a SGS model.

We can see these curves in terms of resolved scales. The numerical scheme introduces dispersion and dissipation errors from a given frequency (cut-off frequency). From now on, we consider a resolved scale as a scale whose wavenumber is below the cut-off frequency. From the dissipation curve we observe that frequencies over the cut-off frequency are naturally dissipated by the numerical method. Following [39], we assume that this dissipation will mimic the high-wavenumber end of the inertial subrange. This will be checked with a numerical example in the following section. In Fig. 3, we observe that the trend of the curves changes around between $\kappa = 3$ and $\kappa = 5$. In fact, the change happens for $\kappa = 4$ (not represented in the figure because it matches the values for $\kappa = 3$). The reason of this behavior lies on the shape of the kernel derivative. The results of a deeper analysis can be found in [53,54].

This approach could be seen in the framework of MILES approach. It is also similar in spirit to the methodology presented in [42] that uses a no-model approach with a numerical method based on quasi-spectral compact finite differences and the addition of an explicit filter. The explicit filter removes the energy of the highest frequencies, and the amount of energy removed is controlled by the parameter of the Padé filter. In our case, the filter is implicitly defined in the numerical model. The filter parameter is the shape parameter of the exponential kernel κ_x. The dissipation curve Fig. 2 (right) gives a flavor of the shape of the implicit

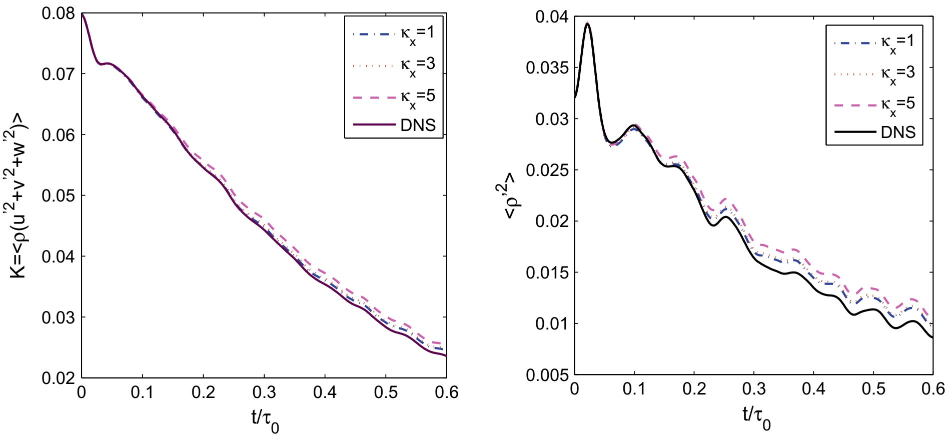

Fig. 8. Effect of the shape parameter κ_x on time history of turbulent kinetic energy decay (left), and on time history of density fluctuations (right). Results on a 64^3 mesh.

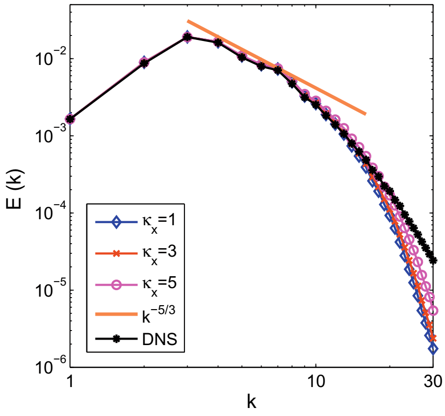

Fig. 9. Instantaneous three-dimensional energy spectra at $t/\tau_0 = 0.3$. Effect of the shape parameter κ_x. Results on a 64^3 mesh.

filter. This approach may also be used on unstructured grids. We remark that other approaches for unstructured grids have been developed [55] with the aim of reducing the extra dissipation introduced by the upwinding (with a stability criteria), and then apply a SGS model. Here we reduce the dissipation introduced by the numerical method by modifying the kernel parameter, but we do not introduce any SGS model.

On the other hand, the effect of the limiter is restricted by the MLS-based shock detector. It allows to keep the high-order of the numerical scheme except in the vicinity of shocks (where it is first-order accurate). Thus, in our approach the shock-capturing is only used to prevent oscillations near shocks. The dissipation is controlled by the κ_x parameter.

One of the advantages of this approach is that there is no need to know in advance if a flow is laminar or turbulent. Moreover, as we will show in the numerical examples, it converges to DNS as the grid is refined. This permits a straightforward treatment of transitional flows.

4. A Numerical example: decay of compressible isotropic turbulence

In this section we solve the problem of the decay of compressible isotropic turbulence. Although this may be the simplest example of turbulent flow, it is usually considered as a test case for both compressible and incompressible formulations of subgrid scale models for LES [56]. Here we reproduce the setup of the problem denoted as Case 6 in [57].

The initial three-dimensional kinetic energy spectrum is defined as:

$$E_{3D} \propto k^4 \exp\left[-2\left(\frac{k}{k_p}\right)^2\right], \tag{40}$$

where k is the magnitude of the wave number vector, and $k_p = 4$ is the wavenumber at the peak of the spectrum.

Following [58], we define χ, as the ratio of compressible kinetic energy to the total turbulent kinetic energy. In this example, $\chi = \left(\frac{q^d}{q}\right)^2 = 0.2$, where q is the root mean square magnitude of the fluctuation velocity, and q^d is the root mean square magnitude of the dilatational fluctuation velocity. We note that χ is an indicator of the level of compressibility of the flow. Thus, $\chi = 0$ corresponds to an incompressible flow.

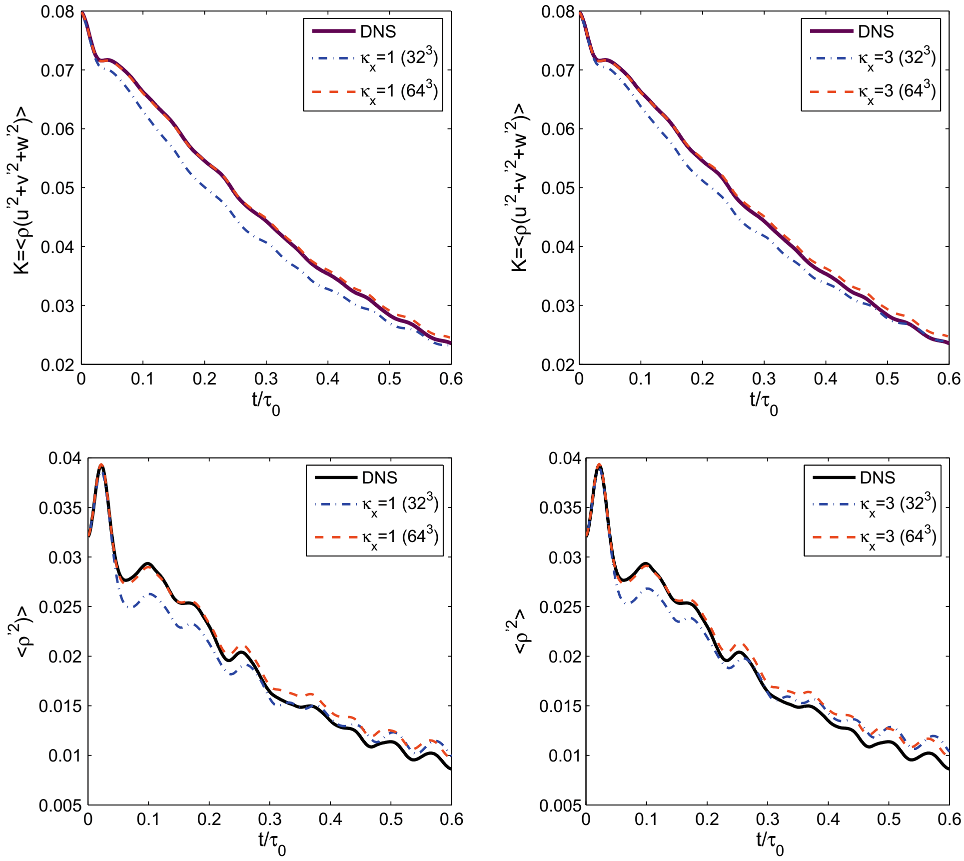

Fig. 10. Convergence under grid refinement. Top: time history of turbulent kinetic energy for $\kappa_x = 1$ (left) and $\kappa_x = 3$ (right). Bottom: time history of density fluctuations for $\kappa_x = 1$ (left) and $\kappa_x = 3$ (right).

The initial velocity fluctuations are specified to obtain a turbulent Mach number, $M_t = \frac{q}{c} = 0.4$, where c is the mean speed of sound. In this simulation, the initial values are given by:

$$\begin{aligned}&(\rho'_{rms})^2\langle\rho\rangle^2 = 0.032\\&(T\prime_{rms})^2/\langle T\rangle^2 = 0.005\end{aligned}\tag{41}$$

The symbol $\langle\rangle$ refers to mean value and primes denote fluctuating variables.

The computational domain is a $2\pi \times 2\pi \times 2\pi$ cube, with periodic boundary conditions. In order to implement the periodicity in the FV-MLS code, we need to modify the stencil of cells close to the periodic boundary. This is schematically represented in Fig. 4. The third-order FV-MLS scheme has been used for the computations, with a MLS-based shock detection technique [48] and the Barth and Jespersen limiter. We have tested two levels of refinement. The coarse grid with 32^3 elements and the finest grid with 64^3 elements. For time integration we use an explicit fourth-order Runge–Kutta scheme. The time step is $\Delta t = 0.05$, corresponding approximately to 250 time-steps per eddy turnover time (τ_0). The eddy turnover time is defined as the ratio of the turbulent kinetic energy to the dissipation rate based on the initial field.

4.1. Results

We start with the computation of a reference solution. This is a LES calculation on a 128^3 grid, computed with sixth-order compact finite differences and a explicit Padé filter with parameter $\alpha = 0.49$, following [42]. As the results of this LES coincide with the DNS of [57], we consider it as the reference solution, to compare with the results of the LES simulation with the FV-MLS method proposed in this paper.

In Figs. 5 and 6 we plot the results obtained on the 32^3 grid, for different values of the kernel shape parameter κ_x. In Fig. 5 we show on the left the time evolution of the turbulent kinetic energy, $K = \langle\rho[(u')^2 + (v')^2 + (w')^2]\rangle$, whereas on the right we plot the time evolution of density fluctuations. Even though the grid is coarse, the results agree very well with those of the reference solution.

In Fig. 6 we show the instantaneous three-dimensional energy spectra at $t/\tau_0 = 0.3$. We note that if we examine the instantaneous three-dimensional spectrum in Fig. 6, we observe that the dissipation introduced affects only to the highest scales of the spectrum. In the 32^3 grid, the highest wavenumber we can represent is $k_c = 16$. For wavenumber $k > 6$, the numerical scheme introduce dissipation (for values of the parameter $\kappa_x \leqslant 3$). Thus, the numerical scheme solves correctly frequencies until a scaled wavenumber of 0.37π. This value of the wavenumber agrees with the behavior predicted in the 1D dissipation curve plotted previously in Fig. 3.

However, for $\kappa_x = 5$ we observe a range of low frequencies with an excess of energy. This feature indicates that this value of the kernel parameter is not optimal, even though the results in the coarser grids follow closely those of the DNS. An important conclusion of this analysis is: even for the coarse grid, the numerical method is able to predict the inertial subrange (see Fig. 6).

It is clear that the choice of κ_x has an influence on the results on the coarser grid. Thus, the value of $\kappa_x = 5$ seems to be somewhat under dissipative. However, the accuracy of the results of the FV-MLS method even in the worst case is greater than the results obtained with fourth-order centered finite differences, as we show in Fig. 7. If we compare with the results of [42], the FV-MLS method clearly improves the results obtained with an standard third-order finite volume scheme.

The results for the finest grid (64^3) elements are plotted in Figs. 8 and 9. Looking at the spectra of Fig. 9, we observe that there is again an excess of energy in the range of the resolved scales $(6 < k < 16)$, for a value $\kappa_x = 5$. This confirms the non optimality of this value of κ_x. In Fig. 10 we compare the results on the two grids. We confirm that the results are consistently better for the finest grid. This is an important conclusion and a remarkable

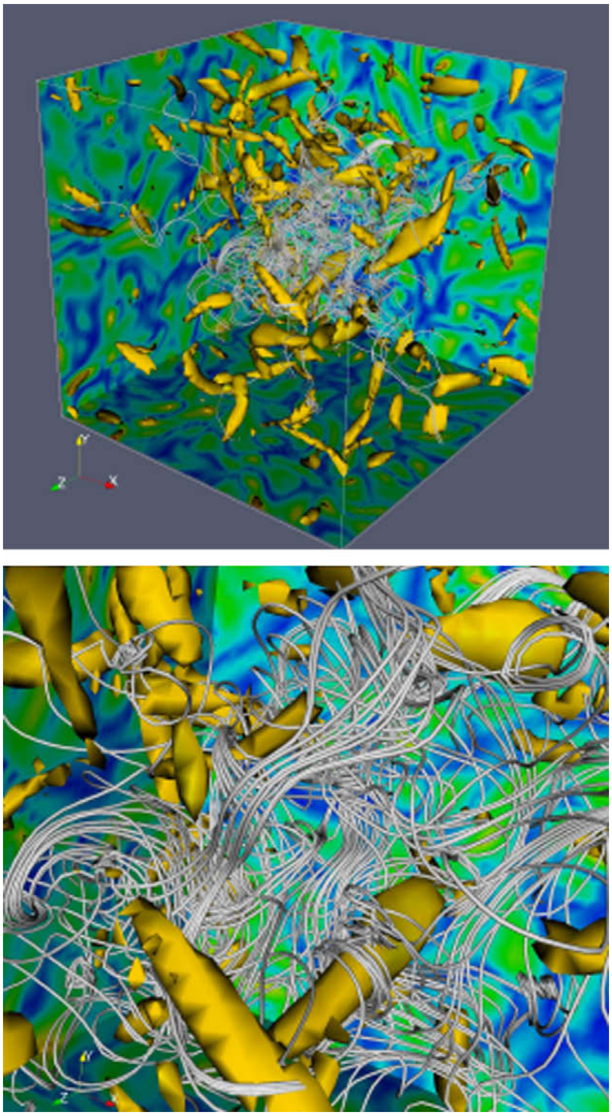

Fig. 11. Isovorticity surfaces and streamlines. General view and detail. Results on a 64^3 mesh.

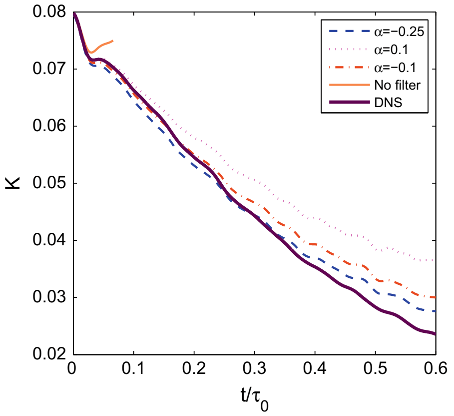

Fig. 12. Time history of turbulent kinetic energy decay. Third-order finite volume method with derivatives computed with sixth-order compact finite differences, with a tenth-order filter of parameter α and without any filter. Results on a 32^3 mesh.

property of this approach. As the grid is refined, the numerical scheme correctly solves the frequencies until a higher wavenumber. Thus, the dissipation is introduced each time in a higher wavenumber, reducing the number of damped scales.

In Fig. 11 we present snapshots of the vorticity isosurfaces, velocity streamlines and vorticity contours. It is observed the presence of the usual vortical structures (*worms*).

Remark 1. We wish to emphasize the importance of the computation of the derivatives in a finite volume framework. The dissipation introduced by an upwind scheme is mainly introduced by dissipation errors in the computation of the derivatives for the reconstruction of the convective terms, and not by the upwinding methodology. In order to do that we solve again the decay of compressible turbulence problem. Now, the derivatives needed for the Taylor reconstruction of the variables inside the cells are computed with sixth-order compact finite differences ([42]). As we reconstruct until the second derivative, the resulting finite volume scheme is third-order accurate. We note that the dissipative fluxes are computed with the MLS reconstruction, so we consider only the effect of the reconstruction of the convective terms. In Fig. 12 we plot the time history of the decay of turbulent kinetic energy. Although the computations have been made with an upwind method, the results are clearly not dissipative. Indeed, we need to use an explicit filter to avoid the pile-up of energy and crashing of the simulation.

In this example, the computation of the derivatives is performed by using a non-dissipative centered scheme. Clearly, the dissipation introduced by the numerical scheme is not enough to act as a SGS model, even though the numerical scheme is upwinded. We can conclude that the dissipation in a finite volume scheme is mainly introduced by the discrete differential operator used for the computation of the derivatives. Thus, an upwind scheme is not necessarily overdissipative. This fact can explain the better results of the FV-MLS method in comparison with other finite volume methods. The quality of the approximated derivatives computed with MLS is superior to usual approaches, and the dissipation is enough to act as a SGS model, but it is not excessive to result in a overdissipative method.

5. Conclusions

We have shown the application of a third-order finite volume method based on Moving Least Squares Approximations to the resolution of turbulent compressible flows. Our approach is based on a ILES approach. We have solved the problem of the decay of compressible turbulence, as a first test case to evaluate the behavior of the third-order FV-MLS method in the resolution of compressible turbulent flows. In order to obtain the monotonicity, a selective limiting technique based on the multiresolution properties of Moving Least Squares approximations have been used. The results obtained are encouraging. The third-order FV-MLS method is able to reproduce the inertial subrange. This is an important result, since not all the numerical methods are able to obtain this results (see [42]). Thus, the numerical method obtains better results than centered fourth-order finite differences, and it really improves the results obtained with the MUSCL scheme. On the other hand, since there is no need to know a priori if the flow is turbulent or not, the present approach is very adequate to the simulation of transitional flows. Finally, it is important to remark that the application of FV-MLS method on unstructured grids is straightforward, being consequently very suitable for the resolution of turbulent flows in complex geometry. However, it is needed to address the issue of non-periodic boundary conditions. Research is in progress to extend the numerical methodology to this kind of problems. Our first results suggest that the use of zero-mean nodes (to improve the quality of stencils) [46] and non-isotropic kernels [47] is a promising approach to solve the difficulties arising from very stretched cells in boundary-layer grids.

Acknowledgments

This work has been partially supported by the *Ministerio de Educación y Ciencia* of the Spanish Government (#DPI2006-15275 and #DPI2007-61214) cofinanced with FEDER funds and the *Secretaría Xeral de I + D* of the *Xunta de Galicia* (Grant #PGDIT06-TAM11801PR). We also acknowledge the collaboration of Dr. D.P. Rizzetta in the complete definition of the decay problem.

References

[1] J.W. Deardorff, A numerical study of three-dimensional turbulent channel flow at large Reynolds numbers, J. Fluid Mech. 41 (2) (1970) 453–480.
[2] J.H. Ferziger, Large Eddy Numerical Simulations of Turbulent Flows, AIAA Paper 76-347, San Diego, CA, 1976.
[3] C.D. Pruett, Eulerian time-domain filtering for spatial large-eddy simulation, AIAA J. 38 (9) (2000) 1634–1642.
[4] J. Smagorinsky, General circulation experiments with the primitive equations. I. The basic experiment, Mon. Weather Rev. 91 (3) (1963) 99.
[5] M. Germano, U. Piomelli, P. Moin, H. Cabot, A dynamic subgrid-scale eddy viscosity model, Phys. Fluids A 3 (7) (1991) 1760–1765.
[6] P. Moin, W. Squires, W. Cabot, S. Lee, A dynamic subgrid-scale model for compressible turbulence and scalar transport, Phys. Fluids A 3 (11) (1991) 2746–2757.
[7] D.K. Lilly, A proposed modification of the germano subgrid-scale closure method, Phys. Fluids A 4 (3) (1992) 633–635.
[8] U. Piomelli, High Reynolds number calculations using the dynamic subgrid-scale stress model, Phys. Fluids A 5 (6) (1993) 1484–1490.
[9] K.S. Yang, J.H. Ferziger, Large-eddy simulation of turbulent obstacle flow using a dynamic subgrid-scale model, AIAA J. 31 (8) (1993) 1406–1413.
[10] J.A. Langford, R.D. Moser, Optimal LES formulations for isotropic turbulence, J. Fluid Mech. 398 (1999) 321–346.
[11] P.S. Zandonade, J.A. Langford, R.D. Moser, Finite-volume optimal large-eddy simulation of isotropic turbulence, Phys. Fluids 16 (7) (2004) 2255–2271.
[12] A. Haselbacher, R. Moser, G. Constantinescu, Toward Optimal LES on Unstructured Meshes, Center for Turbulence Research Proceedings of the Summer Program, Stanford, 2002.
[13] T.J.R. Hughes, L. Mazzei, K.E. Jansen, Large-eddy simulation and the variational multiscale method, Comput. Visual. Sci. 3 (2000) 47–59.
[14] T.J.R. Hughes, L. Mazzei, A.A. Oberai, A.A. Wray, The multiscale formulation of large-eddy simulation: decay of homogeneous isotropic turbulence, Phys. Fluids 13 (2001) 505–512.
[15] T.J.R. Hughes, A.A. Oberai, L. Mazzei, Large-eddy simulation of turbulent channel flows by the variational multiscale method, Phys. Fluids 13 (2001) 1784–1799.
[16] Y. Bazilevs, V.M. Calo, J.A. Cottrell, T.J.R. Hughes, A. Reali, G. Scovazzi, Variational multiscale residual-based turbulence modeling for large eddy simulation of incompressible flows, Comput. Methods Appl. Mech. Engrg. 197 (2007) 173–201.
[17] J. Principe, R. Codina, F. Henkeb, The dissipative structure of variational multiscale methods for incompressible flows, Comput. Methods Appl. Mech. Engrg. (2008), doi:10.1016/j.cma.2008.09.007.
[18] V. Gravemeier, M.W. Geeb, M. Kronbichler, W.A. Wall, An algebraic variational multiscale-multigrid method for large eddy simulation of turbulent flow, Comput. Methods Appl. Mech. Engrg. (2009), doi:10.1016/j.cma.2009.05.017.
[19] F. Van der Bos, J.J.W. Van der Vegt, B.J. Geurts, A multi-scale formulation for compressible turbulent flows suitable for general variational discretization techniques, Comput. Methods Appl. Mech. Engrg. 196 (2007) 2863–2875.
[20] Z. Wang, A.A. Oberai, Spectral analysis of the dissipation of the residual-based variational multiscale method, Comput. Methods Appl. Mech. Engrg. (2009), doi:10.1016/j.cma.2009.06.008.
[21] S. Ramakrishnan, S.S. Collis, Partition selection in multiscale turbulence modeling, Phys. Fluids 18 (7) (2006) 075105.1–075105.16.
[22] S. Stolz, P. Schlatter, D. Meyer, L. Kleiser, High-pass filtered eddy-viscosity models for LES, in: V.R. Friedrich, B.J. Geurts, O. Mtais (Eds.), Direct and Large-Eddy Simulation, Kluwer, Dordrecht, 2003, pp. 81–88.
[23] S. Stolz, High-pass filtered eddy-viscosity models for large-eddy simulations of compressible wall-bounded flows, J. Fluids Engrg. 127 (2005) 666–673.
[24] A.W. Vreman, The filtering analog of the variational multiscale method in large-eddy simulation, Phys. Fluids 15 (8) (2003) L61–L64.
[25] S. Stolz, N.A. Adams, An approximate deconvolution procedure for large-eddy simulation, Phys. Fluids 11 (1999) 1699–1701.
[26] J. Mathew, An explicit filtering method for LES of compressible flows, Phys. Fluids 15 (2003) 2279–2289.

[27] J.A. Domaradzki, K.C. Loh, The subgrid-scale estimation model in the physical space representation, Phys. Fluids 11 (8) (1999) 2330.

[28] M. Terracol, P. Sagaut, C. Basdevanty, A multilevel algorithm for large-eddy simulation of turbulent compressible flows, J. Comput. Phys. 167 (2001) 439–474.

[29] P. Sagaut, Large Eddy Simulation for Incompressible Flows. An Introduction, third ed., Springer, 2005.

[30] J.P. Boris, On large eddy simulation using subgrid turbulence models, in: J.L. Lumley (Ed.), Whither Turbulence? Turbulence at the Crossroads, Springer-Verlag, New York, 1990, pp. 344–353.

[31] J.P. Boris, F.F. Grinstein, E.S. Oran, R.S. Kolbe, New insights into large eddy simulation, Fluid Dyn. Res. 10 (1992) 199–228.

[32] C. Fureby, F.F. Grinstein, Monotonically integrated large eddy simulation of free shear flows, AIAA J. 37 (5) (1999) 544–556.

[33] C. Fureby, F.F. Grinstein, Large eddy simulation of high-Reynolds-number free and wall-bounded flows, J. Comput. Phys. 181 (2002) 68–97.

[34] F.F. Grinstein, C. Fureby, Recent progress on MILES for high Reynolds number flows, J. Fluid Engrg. 124 (2002) 848–861.

[35] N. Adams, The role of deconvolution and numerical discretization in subgrid-scale modeling, in: Geurts, Friedrich, Métais (Eds.), Direct and Large-Eddy Simulation, vol. 4, Kluwer, 2001, pp. 311–320.

[36] P. Beaudan, P. Moin, Numerical Experiments on the Flow Past a Circular Cylinder at Sub-critical Reynolds Numbers, Dept. of Mechanical Engineering, Rept. TF-62, Stanford University, Stanford, CA, 1994.

[37] R. Mittal, P. Moin, Suitability of upwind-biased finite difference schemes for large-eddy simulation of turbulent flows, AIAA J. 35 (8) (1997) 1415–1417.

[38] E. Garnier, M. Mossi, P. Sagaut, P. Comte, M. Deville, On the use of shock-capturing schemes for large-eddy simulation, J. Comput. Phys. 153 (1999) 273–311.

[39] L.G. Margolin, W.J. Rider, A rationale for implicit turbulence modelling, Int. J. Numer. Methods Fluids 39 (2002) 821–841.

[40] D.V. Gaitonde, M.R. Visbal, High-Order Schemes for Navier–Stokes Equations: Algorithm and Implementation into FDL3DI, US Air Force Research Lab, TR AFRL-VA-WP-TR-1998-3060, Wright-Patterson AFB, OH, 1998.

[41] M.R. Visbal, D.V. Gaitonde, High-order-accurate methods for complex unsteady subsonic flows, AIAA J. 37 (10) (1999) 1231–1239.

[42] M.R. Visbal, D.P. Rizzeta, Large-eddy simulation on curvilinear grids using compact differencing and filtering schemes, J. Fluids Engrg. 124 (2002) 836–847.

[43] H. Hoffman, C. Johnson, A new approach to computational turbulence modeling, Comput. Methods Appl. Mech. Engrg. 195 (2006) 2865–2880.

[44] G.S. Karamanos, G.E. Karniadakis, A spectral vanishing viscosity method for large-eddy simulation, J. Comput. Phys. 163 (2000) 22–50.

[45] R. Kirby, G. Karniadakis, Coarse resolution turbulence simulations with spectral vanishing viscosity large-eddy simulations, J. Fluids Eng. 124 (2002) 886–891.

[46] L. Cueto-Felgueroso, I. Colominas, X. Nogueira, F. Navarrina, M. Casteleiro, Finite volume solvers and moving least squares approximations for the compressible Navier–Stokes equations on unstructured grids, Comput. Methods Appl. Mech. Engrg. 196 (2007) 4712–4736.

[47] X. Nogueira, L. Cueto-Felgueroso, I. Colominas, H. Gómez, F. Navarrina, M. Casteleiro, On the accuracy of finite volume and discontinuous Galerkin discretizations for compressible flow on unstructured grids, Int. J. Numer. Methods Engrg. 78 (2009) 1553–1584.

[48] X. Nogueira, L. Cueto-Felgueroso, I. Colominas, F. Navarrina, M. Casteleiro, A new shock-capturing technique based on moving least squares for higher-order numerical schemes on unstructured grids, Comput. Methods Appl. Mech. Engrg., submitted for publication.

[49] P. Lancaster, K. Salkauskas, Surfaces generated by moving least squares methods, Math. Comput. 37 (155) (1981) 141–158.

[50] T.J. Barth, P.O. Frederickson, Higher-order Solution of the Euler Equations on Unstructured Grids Using Quadratic Reconstruction, AIAA Paper 90-0013, 1990.

[51] T.J. Barth, D.C. Jespersen, The Design and Application of Upwind Schemes on Unstructured Meshes, AIAA-89-0366, 1989.

[52] G.R. Liu, M.B. Liu, Smoothed Particle Hydrodynamics. A Meshfree Particle Method, World Scientific Publishing, Singapore, 2003.

[53] X. Nogueira, Moving Least Squares and High-order Finite Volume Methods For the Numerical Simulation of Compressible Flows, Ph.D. Thesis, Universidade da Coruña, 2009 (in Spanish). <http://www.tdr.cesca.es>.

[54] X. Nogueira, L. Cueto-Felgueroso, I. Colominas, S. Khelladi, On the simulation of wave propagation with a higher-order finite volume scheme based on reproducing Kernel methods, Comput. Methods Appl. Mech. Engrg., submitted for publication.

[55] M. Ciardi, P. Sagaut, M. Klein, W.N. Dawes, A dynamic finite volume scheme for large-eddy simulation on unstructured grids, J. Comput. Phys. 210 (2005) 632–655.

[56] K.E. Jansen, A stabilized finite element method for computing turbulence, Comput. Methods Appl. Mech. Engrg. 174 (1999) 299–317.

[57] E.T. Spyropoulos, G.A. Blaisdell, Evaluation of the dynamic model for simulations of compressible decaying isotropic turbulence, AIAA J. 34 (5) (1996) 990–998.

[58] S. Sarkar, G. Erlebacher, M.Y. Hussaini, H.O. Kreiss, The analysis and modelling of dilatational terms in compressible turbulence, J. Fluid Mech. 227 (1991) 473–493.